

# Ultrafast element-resolved magneto-optics using a fiber-laser-driven extreme ultraviolet light source

Christina Möller,<sup>1,2</sup> Henrike Probst,<sup>1,2</sup> Johannes Otto,<sup>1,2, a)</sup> Karen Stroh,<sup>1,2</sup> Carsten Mahn,<sup>1,2</sup> Sabine Steil,<sup>1,2</sup> Vasily Moshnyaga,<sup>1,2</sup> G. S. Matthijs Jansen,<sup>1,2</sup> Daniel Steil,<sup>1,2</sup> and Stefan Mathias<sup>1,2, b)</sup>

<sup>1)</sup>*I. Physikalisches Institut, Universität Göttingen, Friedrich-Hund-Platz 1, 37077 Göttingen, Germany*

<sup>2)</sup>*International Center for Advanced Studies of Energy Conversion (ICASEC), Georg-August-Universität Göttingen, 37077, Göttingen, Germany*

We present a novel setup to measure the transverse magneto-optical Kerr effect in the extreme ultraviolet spectral range at exceptionally high repetition rates based on a fiber laser amplifier system. This affords a very high and stable flux of extreme ultraviolet light, which we use to measure element-resolved demagnetization dynamics with unprecedented depth of information. Furthermore, the setup is equipped with a strong electromagnet and a cryostat, allowing measurements between 10 and 420 K using magnetic fields up to 0.86 T. The performance of our setup is demonstrated by a set of temperature- and time-dependent magnetization measurements showing distinct element-dependent behavior.

## I. INTRODUCTION

In the last decades, magneto-optical spectroscopy has led to an impressive series of discoveries in ultrafast magnetism, spanning from the discovery of optically-induced ultrafast manipulation of magnetic order<sup>1,2</sup> to the experimental verification of the theoretically-predicted existence of femtosecond spin currents<sup>3–5</sup> and optically-induced spin transfer<sup>6–13</sup>. Nevertheless, a complete and thorough understanding of the phenomena on a microscopic scale is still an area of active research. Here, the use of ultrashort extreme ultraviolet (EUV) light pulses to probe the instantaneous magnetization enables both few femtosecond time-resolution and the possibility to disentangle the contributions of individual elemental components of the probed system<sup>14,15</sup>. Making use of the transverse magneto-optical Kerr effect (T-MOKE), full time- as well as energy-resolved (and thus element-resolved) data can be acquired from the wavelength-dependent reflection of the sample<sup>9,16,17</sup>.

A commonly used light source for both magnetic<sup>8,16,18,19</sup> and non-magnetic<sup>20</sup> extreme ultraviolet spectroscopy is high-harmonic generation (HHG)<sup>21,22</sup>. HHG combines a compact, laboratory-scale light source with excellent properties of the EUV light; namely a high degree of coherence, broad bandwidth and ultrashort pulse durations in the low-femtosecond to attosecond regime, allowing state-of-the-art time resolution in pump-probe experiments. In comparison to alternative short-pulse EUV light sources such as free-electron lasers<sup>23</sup> and femtoslicing synchrotrons<sup>24,25</sup>, generation of a stable EUV source with high average power is challenging. In that regard, several approaches based on high-repetition-rate, high-power lasers have recently been developed<sup>26,27</sup>. Up until now however, laboratory-based extreme ultraviolet magneto-optic experiments have been limited by the use of Ti:Sapphire laser systems at repetition rates below a few ten

kilohertz<sup>8,16–19</sup>.

In this article, we present a novel EUV T-MOKE experiment providing massively improved signal quality due to the use of a high-repetition-rate fiber laser system to drive the high-harmonic generation. Amongst others, our photon energy range of 30 to 72 eV covers the  $M_{2,3}$  absorption edges of the  $3d$  transition metals Co, Ni, Fe and Mn, allowing a simultaneous probing of magnetic properties of these elements. In contrast to earlier HHG-based femtomagnetism experiments, we operate at much higher repetition rates up to 300 kHz, which allows for extremely high signal quality in only limited acquisition time. Furthermore, we are able to apply high magnetic fields of up to 0.86 T and temperatures between 10 K and 420 K in our setup.

## II. SETUP FOR TIME-RESOLVED T-MOKE AT EUV WAVELENGTHS

The experiment makes use of the transverse magneto-optical Kerr effect (T-MOKE) to measure the magnetization of the sample. In T-MOKE, the sample magnetization is aligned parallel to the sample surface and perpendicular to the plane of incidence of the light. Here, a magnetization-dependent change in the reflectivity can be observed for p-polarized light. As this can be measured by a simple intensity measurement, T-MOKE is especially well-suited in the EUV spectral range, where polarization analysis is non-trivial<sup>28</sup>.

The quantity accessible by T-MOKE is the magnetic asymmetry  $A$ , which is the difference in reflected intensity from the sample for both magnetization directions ( $I_{\uparrow}$  and  $I_{\downarrow}$ ), normalized to the sum of the intensities

$$A = \frac{I_{\uparrow} - I_{\downarrow}}{I_{\uparrow} + I_{\downarrow}} \approx 2\text{Re} \left[ \frac{\sin(2\theta_0)\epsilon_{xy}}{n^4 \cos^2 \theta_0 - n^2 + \sin^2 \theta_0} \right]. \quad (1)$$

The index of refraction  $n$  and the off-diagonal elements of the dielectric tensor  $\epsilon_{xy}$  describe the reaction of the full quantum-mechanical system to the incident light field, and can be calculated by considering all possible electronic transitions for the material's spin-resolved band structure and instantaneous electron occupation.<sup>17,29</sup> As a result, both  $n$  and  $\epsilon_{xy}$

<sup>a)</sup>current address: IV. Physikalisches Institut, Universität Göttingen, Friedrich-Hund-Platz 1, 37077 Göttingen, Germany

<sup>b)</sup>Electronic mail: smathias@uni-goettingen.de

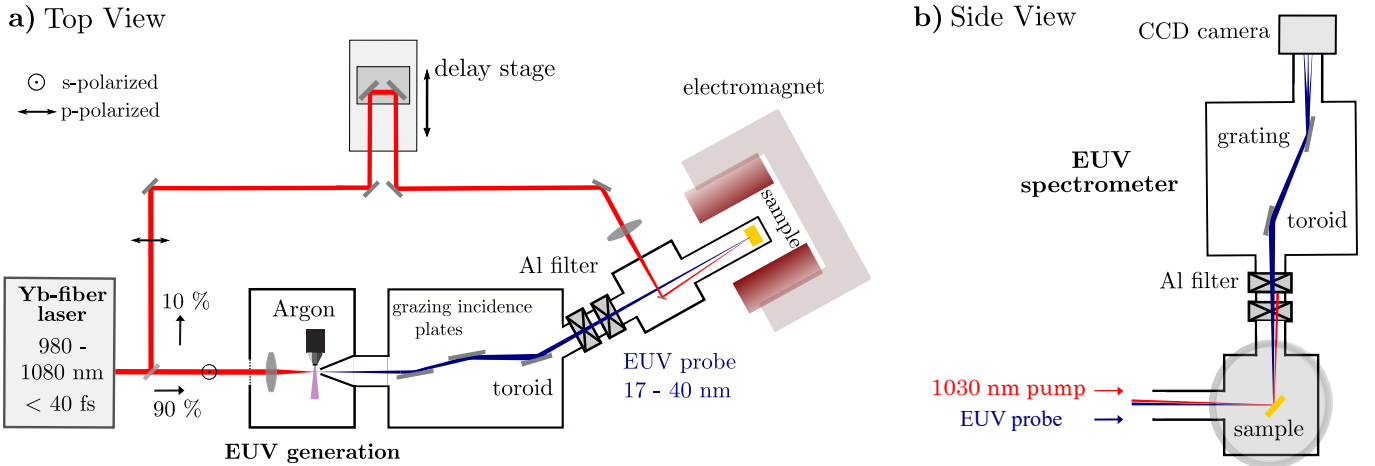


FIG. 1. Schematic overview of the setup: a) top view: High harmonics are generated in an argon gas jet by intense IR pulses at a repetition rate up to 300 kHz. The fundamental beam is consequently filtered out by two grazing incidence plates and an Al filter. The toroidal mirror focuses the EUV beam onto the sample inside the electromagnet. b) side view: After reflection on the sample, the high harmonic spectrum is analyzed by our custom-built spectrometer composed of a toroidal mirror, a grating and a CCD camera. The pump beam is coupled into the vacuum chamber and blocked by a second Al filter after reflection on the sample.

are wavelength-dependent, and change rapidly near absorption edges. In particular, resonant enhancement of  $\epsilon_{xy}$  at the M edges of transition metals<sup>30,31</sup> combined with a general enhancement of the magnetic asymmetry at absorption edges<sup>15</sup> leads to a strong, wavelength-dependent T-MOKE signal in the EUV range for the  $3d$  transition metals. Here, spectroscopy can be optimally used to disentangle elemental contributions from the magnetic asymmetry.

In the second step of Eq. 1, the magnetic asymmetry was approximated by inserting the expressions for  $p$ -polarized reflected intensities under the assumption that the Fresnel coefficient is large compared to the magneto-optical term.<sup>15</sup> Higher order terms of the magnetization-dependent off-diagonal element of the dielectric tensor  $\epsilon_{xy}$  are neglected. From this expression, it can be deduced that, in thermal equilibrium, the asymmetry is proportional to the magnetization inside the sample. The expression is maximized when the denominator approaches zero. This is exactly the case for  $\tan \theta_0 = n$ , which is the condition for the Brewster angle. Since  $n \approx 1$  in the EUV range, the optimal angle of incidence corresponds to  $\theta_0 = 45^\circ$ .

### A. The fiber-laser HHG light source

Here, we present a T-MOKE setup using EUV light from a high-harmonic generation (HHG) light source to probe the sample. Ultrafast (de)magnetization dynamics are induced by tuneable pump pulses from the same high repetition-rate fiber laser system used to drive the HHG. After reflection from the sample, the EUV light is dispersed in a custom-built spectrometer and the diffracted harmonics are detected by a CCD camera. A schematic overview of the setup is shown in Fig. 1.

Ultrashort laser pulses with a center wavelength of 1030 nm, tuneable repetition rate up to 300 kHz, pulse energy

of up to 150  $\mu\text{J}$  and pulse lengths below 40 fs are generated by a fiber laser system (Active Fiber Systems). This is achieved by self-phase modulation of 300 fs pulses from an ytterbium-doped fiber amplifier in a krypton-filled hollow-core fiber and subsequent compression by chirped mirrors. The beam is split into a pump and a probe beam by a variable attenuator, consisting of a  $\lambda/2$ -plate and two broadband thin film polarizers. The s-polarized output of the attenuator is focused by a 100 mm focal length lens into an argon gas jet to generate high harmonics, which provides the probe beam in our experiment. In order to optimize the HHG process, the gas jet is mounted on a 3-axis positioning system. Efficient HHG was observed at an argon backing pressure of 17 bar for a gas nozzle diameter of 100  $\mu\text{m}$ .

To minimize reabsorption of the generated EUV beam, the chamber is pumped by a multi-stage root pump (Ebara EV-SA30) and a 1 mm differential pumping aperture is placed directly behind the generation point. This results in a pressure of  $2 \times 10^{-4}$  mbar in the subsequent mirror chamber despite the quite high gas load in the first chamber (1.1 mbar). The generated high harmonics are separated from the fundamental by two grazing-incidence plates (GIP) inside the mirror chamber.<sup>32</sup> These fused silica plates are anti-reflection coated for 1030 nm on the front and backside, whereby most of the fundamental beam is transmitted and dumped outside the vacuum chamber. An additional top  $\text{Ta}_2\text{O}_5$  coating of the GIP allows for a high reflection of the EUV spectrum at  $10^\circ$  grazing incidence. After the GIPs, a  $\text{B}_4\text{C}$ -coated toroidal mirror (276 mm focal length at  $15^\circ$  grazing incidence angle) focuses the probe beam onto the sample in a  $350 \times 100 \mu\text{m}^2$  spot ( $1/e^2$ -diameter). The EUV light then passes a 100 nm thick aluminum filter which is mounted in front of the sample in a VAT valve to block any residual fundamental light.

## B. Pump beamline

A second variable attenuator in the pump beamline allows for manipulation of the pump beam intensity. A motorized delay line changes the optical path length with respect to the probe path. After passing a 350 mm focal length lens, the pump beam is coupled into the vacuum chamber such that the angle between the pump and the EUV beamline is less than  $2^\circ$ . The beam diameter at the sample position was determined to be  $760 \times 720 \mu\text{m}^2$ , yielding a pump fluence of  $1.75 \text{ mJ}/\text{cm}^2$  for an average power of 750 mW at a repetition rate of 100 kHz. The pulse duration is measured by intensity autocorrelation to be 58 fs, assuming a Gaussian pulse shape. The pump beam is s-polarized with respect to the plane of incidence on the sample for the measurements shown in this paper.

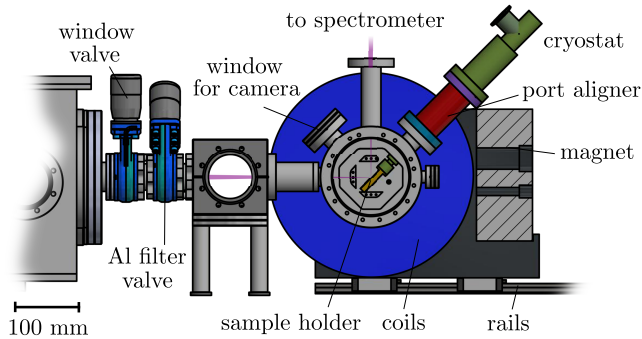


FIG. 2. Technical drawing of the custom-built sample chamber, providing a view directly into the sample chamber.

## C. Sample environment

The sample environment is a custom-made chamber based on a CF150 flange and designed to fit in the 45 mm wide pole gap of the electromagnet (see Fig. 2). The flange can be opened from the side, which enables easy access to the sample. For this purpose the electromagnet surrounding the sample chamber is mounted on rails, allowing to remove the magnet and providing unobstructed access to the sample chamber. The switching time of the electromagnet varies from 60 ms for 100 mT up to 600 ms for the maximum field strength of 860 mT.

The samples are mounted on a removable copper sample holder attached to a cryostat, which is fixed at a  $45^\circ$  angle with respect to the incoming pump and probe beams. In order to make small changes to the position and angle of the sample, the cryostat is attached to the chamber with an ultrahigh vacuum (UHV) port aligner. The continuous-flow UHV cryostat (Janis Research ST400) enables temperature control of the sample in the range of  $\approx 10$  to 420 K. Typically, the pressure inside the chamber is below  $1 \times 10^{-7}$  mbar during operation, however, even UHV conditions can be achieved by baking out the vacuum chamber.

To verify spatial overlap of the pump and probe beam, the diffuse reflection of the pump and fundamental of the high

harmonics on the sample is imaged with a CMOS sensor. The temporal overlap is achieved by observing sum frequency generation of both IR pulses in a beta barium borate (BBO) crystal at the sample position or recording interference fringes with a beam profiler. Both of these methods can be performed outside of the vacuum system by inserting a moveable mirror directly in front of the sample. This determination of the temporal overlap is limited by a small difference in the optical path lengths of the fundamental and the high harmonics. Therefore, a final determination of the temporal overlap is done by searching for the onset of demagnetization as probed by the EUV light.

## D. Spectrometer design

Spectroscopy of the reflected EUV light allows for the investigation of the sample magnetization and is realized by a custom-built spectrometer based on a plane grating as the dispersive element and a toroidal mirror as the focusing element. The spectrometer was designed to achieve a high energy resolution to distinguish between the individual harmonics and to provide in-detail access to spectrally distinct dynamics around the absorption edges of the different elements.

The sample reflects both the pump and probe beams towards the spectrometer chamber (see Fig. 1b). Here, a second aluminum filter is introduced into the beam path to block the reflected pump beam. The EUV beam is focused towards the CCD-camera (GE 2048 512 BI UV, Greateyes) by a toroidal mirror, which is identical to the toroidal mirror used to focus the EUV probe beam on the sample. The planar reflection grating is positioned in the off-plane geometry, where the grating grooves lie parallel to the plane of incidence of the light. An advantage of this geometry is that it allows for the use of efficient blazed gratings while maintaining the low grazing incidence angle which is necessary for high reflectivities at EUV wavelengths<sup>33</sup>. The grating is gold-coated and has a groove density of 1800 lines/mm. Given the blaze angle  $\delta$  of  $9.3^\circ$ , optimal diffraction efficiency is achieved at the altitude angle  $\gamma$  of  $6.5^\circ$  for wavelengths near the M-edges of the  $3d$  ferromagnets. To prevent camera exposure during the sensor readout procedure, a shutter is positioned between the toroidal mirror and the grating.

A consequence of this spectrometer design is that the EUV wavefront incident on the grating is curved. Equivalently, it can be said that the azimuth angle  $\theta$  and the altitude angle  $\gamma$  of the beam on the grating have a certain spread. This will lead to a distortion of the measured spectrum, which is calculated here. The grating equation for this system is<sup>34</sup>

$$m\lambda\sigma = \sin\gamma(\sin\theta - \sin\theta'), \quad (2)$$

where  $m$  is the diffraction order,  $\lambda$  the wavelength,  $\sigma$  the grating constant and  $\theta'$  the exit angle. Substituting  $\theta \rightarrow \theta_0 + \Delta\theta$  and  $\gamma \rightarrow \gamma_0 + \Delta\gamma$  and performing a Taylor expansion around  $\Delta\theta = \Delta\gamma = 0$ , we find

$$\theta' = \theta'_0 - c_1\Delta\theta + c_2\Delta\gamma + O(\Delta\theta^2 + \Delta\theta\Delta\gamma + \Delta\gamma^2). \quad (3)$$

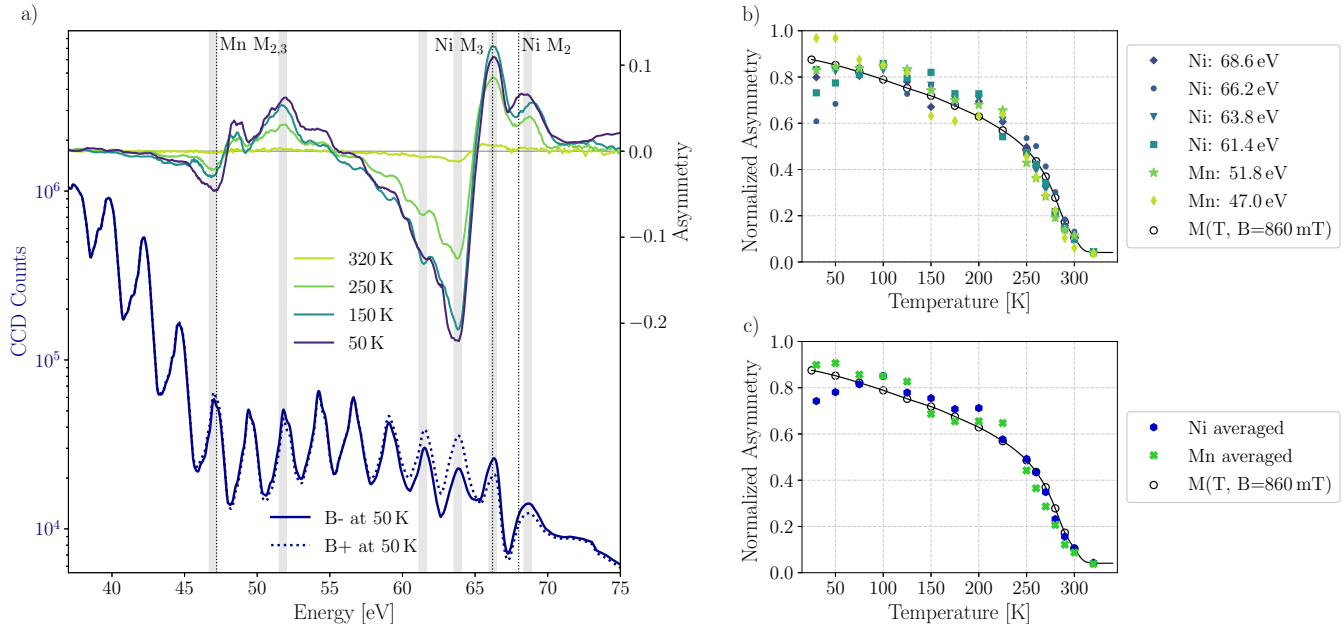


FIG. 3. Temperature dependence of the magnetic asymmetry of the LNMO phase transition. a) The magnetic asymmetry, together with typical HHG spectra at 50 K for the different magnetization directions. b) Temperature-dependent magnetic asymmetry for 0.5 eV energy intervals around the relevant high harmonic energies of Mn and Ni. c) The magnetic asymmetry traces for Mn and Ni, averaged over all relevant high harmonics. The asymmetry traces in (b) and (c) nicely follow the  $M(T, B = 860 \text{ mT})$  data points which were recorded using SQUID magnetometry. The black line is an interpolation of the  $M(T, B = 860 \text{ mT})$  data and serves as a guide to the eye.

In our experimental geometry,  $c_1 \approx 1.1$  and  $c_2$  is typically on the order of 3. Higher order terms can be ignored because they are typically one to two orders of magnitude weaker than the linear terms. From this result, we can conclude the following: 1) the term linear in  $\Delta\theta$  will increase the wavefront curvature, leading to an astigmatic focus of the diffracted beam. On the camera, this results in spots which are elongated perpendicular to the spectral direction. 2) the term linear in  $\Delta\gamma$  will shift the diffracted beams depending on their altitude angle. Effectively, this leads to a grating dispersion which is stronger for shallower grazing incidence angles on the grating.

In order to correct for this deformation of the measured spectrum, we first transform the cartesian coordinates of the camera onto a  $(\theta, \gamma)$ -coordinate system. Next, we apply a  $\gamma$ -dependent scaling of the diffraction angle, eliminating the tilt of the high harmonics. Finally, we integrate the two-dimensional measurement along the spatial dimension without loss of spectral resolution.

In daily operation, the aluminum  $L_3$  edge at 72.7 eV and the known separation of the high harmonics by twice the fundamental frequency are used to calibrate the energy of the recorded high harmonics. In addition, the energy calibration of the spectrum is verified by inserting a 200 nm thick tin filter, which transmits EUV light up to 23.6 eV allowing to identify the 19<sup>th</sup> harmonic (22.9 eV) of our fundamental driver.

### III. EXEMPLARY EXPERIMENTAL RESULTS AND ANALYSIS

In the following, we present temperature- and time-dependent measurements of the magnetic asymmetry. The results show the ferromagnetic phase transition of  $\text{La}_2\text{NiMnO}_6$  and the distinct ultrafast magnetization dynamics of iron and nickel in a  $\text{Fe}_{19}\text{Ni}_{81}$  alloy. These measurements demonstrate the capabilities of our setup to record magnetization traces with a high signal-to-noise ratio over a broad range of sample temperatures between 10 and 420 K and with femtosecond time resolution.

#### A. Temperature-dependent magnetic asymmetry

Thin-film perovskite manganites exhibit rich phase diagrams due to the strong correlations between charge, lattice and spin degrees of freedom<sup>35–37</sup>, which can be of particular interest for ultrafast spin dynamics. Here, we investigated the ferromagnetic to paramagnetic phase transition in the double perovskite  $\text{La}_2\text{NiMnO}_6$  (LNMO). The magnetic asymmetry was recorded in a temperature range of 30 K to 320 K. Typical HHG spectra at 50 K for both magnetization directions and the resulting asymmetry spanning the  $M_{2,3}$  absorption edges of manganese (47.2 eV) and nickel (66.2 eV and 68 eV) for different temperatures are depicted in Fig. 3a. The measurements were performed in an applied magnetic field of 860 mT. For each temperature, 500 spectra with an exposure time of 1

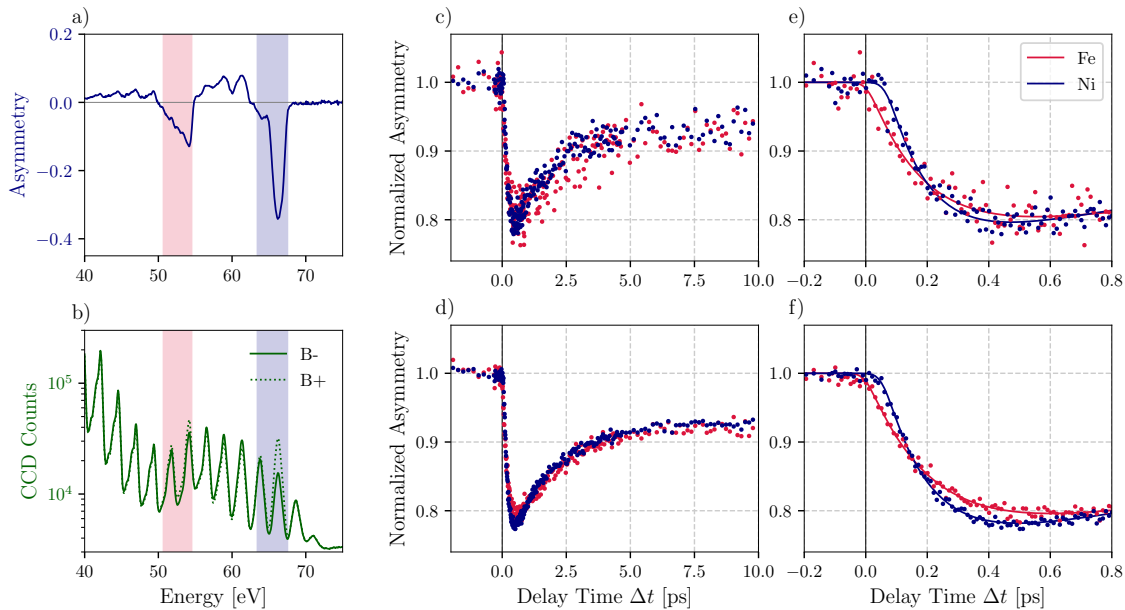


FIG. 4. Time-resolved demagnetization measurement of  $\text{Fe}_{19}\text{Ni}_{81}$  for a short (1 hour) and long (12 hours) time measurement. a) Typical magnetic asymmetry of the sample before arrival of the pump pulse. b) Corresponding high-harmonic spectra for both magnetic field directions. c, d) Relative demagnetization time traces for iron and nickel for one and twelve hours measurement time respectively. Here, the asymmetry is averaged over the depicted energy intervals in (a) and normalized to time delays before time zero. e, f) Zoom-in on the short-timescale dynamics of (c) and (d) respectively. The solid lines are least-square fits according to a double exponential function (eq. (4)), the results of which are given in table I.

second per magnetization direction were recorded. In order to analyze the quantitative temperature dependence of the asymmetry, we calculated the mean asymmetry in a 0.5 eV energy interval around the relevant high harmonic peaks for Mn and Ni, indicated by the shaded areas in Fig. 3a. As a reference, we extracted the sample magnetization at  $B = 860$  mT from full hysteresis curves  $M(B)$  in the temperature range of 5-300 K as measured using a superconducting quantum interference device (SQUID) magnetometer. In order to compare the observed magnetic asymmetry to the  $M(T, B = 860$  mT) data, we have normalized the magnetic asymmetry to the sum of the asymmetry values for all temperatures and then scaled it with the magnetization  $M(T, B = 860$  mT) integrated over the full temperature range.

The temperature-dependent magnetic asymmetry for all relevant harmonic peaks is shown together with the  $M(T, B = 860$  mT) data in Fig. 3b. The normalized asymmetry values for Mn and Ni show good agreement with the  $M(T, B = 860$  mT) reference measurement performed with SQUID across the entire temperature range. The expected loss of magnetization with increasing temperature is clearly visible. The remaining non-negligible magnetization beyond the phase transition in Fig. 3b is induced by the strong external field of 860 mT applied during the measurement and evident in both the T-MOKE measurement and SQUID  $M(T, B = 860$  mT) data.

To extract a mean value of the magnetic asymmetry for both Mn and Ni, we averaged the asymmetry of the relevant harmonics for both elements. The resulting averaged mag-

netic asymmetry traces are shown in Fig. 3c. From the overall agreement between the EUV magnetic asymmetry measurement and the SQUID measurement, we conclude that static EUV T-MOKE effectively probes the bulk magnetization in the steady state.

## B. Time-resolved EUV-T-MOKE

To demonstrate the performance of our setup we recorded the time evolution of the ultrafast demagnetization in a  $\text{Fe}_{19}\text{Ni}_{81}$  thin film at 100 mT applied field. Ultrafast demagnetization is initiated by a 58 fs, 1.2 eV pump pulse (measured by autocorrelation, assuming Gaussian pulse shape). The absorbed pump fluence is  $\approx 0.7$  mJ/cm<sup>2</sup>. At this fluence, the 700 mW thermal load on the sample leads to a limited thermal demagnetization of around 5 % for our pulse repetition rate of 100 kHz. The measurement time was 12 hours which corresponds to 96 0.7-second measurements of the asymmetry per delay position. We will compare the results from this long integration to results from shorter integration slices selected from this data.

The results are summarized in Fig. 4, including recorded EUV spectra for both magnetization directions after subtraction of a background image, the resulting asymmetry according to equation (1), and the time dependence of the normalized magnetic asymmetry for a 12-hour measurement as well as an exemplary 1-hour data set selected from the long measurement. For the time-dependent data, the magnetic asymmetry

Fe, 50.7 to 54.5 eV	1 hour	12 hours
$t_0$ (fs)	$7 \pm 10$	$0 \pm 3$
$\Delta A_m$	$0.253 \pm 0.012$	$0.276 \pm 0.005$
$\Delta A_r$	$0.182 \pm 0.010$	$0.199 \pm 0.004$
$\tau_m$ (fs)	$185 \pm 21$	$214 \pm 8$
$\tau_r$ (ps)	$1.96 \pm 0.24$	$1.85 \pm 0.08$
Ni, 63.4 to 67.5 eV	1 hour	12 hours
$t_0$ (fs)	$67 \pm 5$	$55.2 \pm 1.9$
$\Delta A_m$	$0.264 \pm 0.008$	$0.279 \pm 0.003$
$\Delta A_r$	$0.197 \pm 0.007$	$0.206 \pm 0.003$
$\tau_m$ (fs)	$137 \pm 10$	$147 \pm 4$
$\tau_r$ (ps)	$1.5 \pm 0.1$	$1.67 \pm 0.04$

TABLE I. Fit results using Eq. 4 of the demagnetization traces in Fig. 4. For the least-squares fit, measurement data were weighted according to the data spread at each delay individually. The given error margins correspond to the 1-sigma standard deviations of the fit.

was averaged over the indicated energy intervals in Fig. 4a. Negative time delays indicate that the EUV pulse probes the sample before the pump pulse arrives.

For the analysis of the raw asymmetry data, large energy regions around the M absorption edges were chosen: Fe between 50.7 and 54.5 eV and Ni between 63.4 and 67.5 eV. By integrating the off-diagonal component of the dielectric tensor over a wider energy range, we are less sensitive to spectrally distinct band-structure renormalization and population dynamics<sup>9,10,17,38–41</sup>, and we effectively probe the element-specific magnetization. Already from the 1-hour dataset, we can easily resolve the delayed demagnetization dynamics between nickel and iron, as previously seen in Refs. 9, 18, 42, and 43, which highlights the excellent signal-to-noise ratio of our setup.

In order to do a quantitative analysis of the data, we fit the time evolution of the asymmetry for both energy intervals using a double-exponential function convolved with a Gaussian function  $G(t)$  with a full width at half maximum of 58 fs:

$$\frac{A(t)}{A(t < t_0)} = G(t) \otimes \left[ 1 - \Theta(t - t_0) \cdot \left[ \Delta A_m \cdot \left( 1 - e^{-\frac{t-t_0}{\tau_m}} \right) - \Delta A_r \cdot \left( 1 - e^{-\frac{t-t_0}{\tau_r}} \right) \right] \right].$$

Here,  $t_0$  defines the onset of the demagnetization process,  $\tau_m$  and  $\tau_r$  are the demagnetization and remagnetization constants, respectively,  $\Delta A_m$  is proportional to the maximal fractional demagnetization, and  $\Delta A_r$  is proportional to the fast remagnetization. For our data,  $\Delta A_r$  is smaller than  $\Delta A_m$ , meaning that the sample does not return to its ground state in the measured 10-ps time range. Full remagnetization is only achieved on a longer timescale. The least-square fit results are listed in table I. In addition to the delayed dynamics in nickel, we observe a faster demagnetization time at the nickel M-edge as well as a slightly stronger demagnetization for the selected spectral ranges.

Crucially, the fit results for the 1-hour data set differ only

slightly from the results for the complete 12-hour data. The differences in demagnetization dynamics between iron and nickel are well-reproduced by this much shorter measurement. To verify that these results are not simply by choice of our 1 hour data set, we split the 12-hour data set in one-hour chunks and repeated the least-square fit for each of these. From this analysis, we find that generally, the 1-hour fit results closely match with the 12-hour result. However, the predicted error margins from a single least-square fit underestimate the true variance of the analysis results by roughly a factor two. For example for the onset of demagnetization in nickel, we find values centered on 53 fs with a 1-sigma standard deviation of 9 fs. Such differences are acceptably small however, and can easily be explained by small drifts in the experimental setup over the course of the long measurement.

#### IV. CONCLUSION

In summary, we have presented a novel setup combining a high-repetition-rate bright high harmonic light source with a T-MOKE-setup enabling high magnetic fields up to 0.86 T and sample temperatures down to 10 K. We have shown that this setup allows for the detailed measurement of element-specific magnetization behavior in complex samples such as the double perovskite LNMO. Furthermore, using a  $\text{Fe}_{19}\text{Ni}_{81}$  permalloy thin film as a well-known reference sample, we have demonstrated the capabilities of our setup to measure high-quality ultrafast demagnetization dynamics. We find that already a single hour of measurement time allows for a detailed view into the ultrafast dynamics in a 10-picosecond time window. For example, this measurement already allows us to determine the relative delay of the demagnetization in nickel compared to iron with 10 fs accuracy. Extending our measurement to 12 hours, we acquire excellent data with very low noise, which can be directly attributed to the use of the high-power Yb-fiber laser, operating at 100 to 300 kHz repetition rate.

In the future, we will apply our setup to the measurement of element-resolved magnetic responses as a function of temperature, time and magnetic field. Amongst others, this work will contribute to a more profound microscopic understanding of the dynamics in complex magnetic alloys and strongly correlated electron systems.

#### V. ACKNOWLEDGEMENTS

H.P, K.S, S.M., V.M. and D.S. acknowledge support from the German Science Foundation through project number 399572199. G.S.M.J. acknowledges funding by the Alexander von Humboldt Foundation. We thank Manfred Albrecht from the University of Augsburg for the fabrication of the Permalloy sample. Also, we wish to thank Christof Schmidt and the team of the central workshop of physics for their excellent support in constructing the HHG EUV-T-MOKE setup.

## VI. DATA AVAILABILITY

The data that support the findings of this study are available from the corresponding author upon reasonable request.

## VII. SAMPLE PREPARATION

The double perovskite LNMO film with a thickness of  $d \approx 100$  nm was epitaxially grown on a MgO(100) substrate by means of a solution-based and vacuum-free metalorganic aerosol deposition (MAD) technique<sup>44</sup>.

The investigated Fe<sub>19</sub>Ni<sub>81</sub> sample is a 15-nm thin film deposited with magnetron sputtering at room temperature on a silicon substrate (Si/SiO<sub>2</sub>(100 nm)) and capped with 5 nm Si<sub>3</sub>N<sub>4</sub>. The sample is poly-crystalline and exhibits an in-plane magnetization orientation.

## VIII. REFERENCES

- <sup>1</sup>E. Beaurepaire, J.-C. Merle, A. Daunois, and J.-Y. Bigot, "Ultrafast spin dynamics in ferromagnetic nickel," *Physical review letters* **76**, 4250 (1996).
- <sup>2</sup>A. Kirilyuk, A. V. Kimel, and T. Rasing, "Ultrafast optical manipulation of magnetic order," *Rev. Mod. Phys.* **82**, 2731–2784 (2010).
- <sup>3</sup>M. Battiato, K. Carva, and P. M. Oppeneer, "Superdiffusive spin transport as a mechanism of ultrafast demagnetization," *Phys. Rev. Lett.* **105**, 027203 (2010).
- <sup>4</sup>D. Rudolf, C. La-O-Vorakiat, M. Battiato, R. Adam, J. M. Shaw, E. Turgut, P. Maldonado, S. Mathias, P. Grychtol, H. T. Nembach, T. J. Silva, M. Aeschlimann, H. C. Kapteyn, M. M. Murnane, C. M. Schneider, and P. M. Oppeneer, "Ultrafast magnetization enhancement in metallic multilayers driven by superdiffusive spin current," *Nature Communications* **3**, 1037 (2012).
- <sup>5</sup>E. Turgut, C. La-O-Vorakiat, J. M. Shaw, P. Grychtol, H. T. Nembach, D. Rudolf, R. Adam, M. Aeschlimann, C. M. Schneider, T. J. Silva, M. M. Murnane, H. C. Kapteyn, and S. Mathias, "Controlling the competition between optically induced ultrafast spin-flip scattering and spin transport in magnetic multilayers," *Physical Review Letters* **110**, 1–6 (2013).
- <sup>6</sup>P. Elliott, T. Müller, J. K. Dewhurst, S. Sharma, and E. K. U. Gross, "Ultrafast laser induced local magnetization dynamics in Heusler compounds," *Sci. Rep.* **6**, 38911 (2016).
- <sup>7</sup>J. K. Dewhurst, P. Elliott, S. Shallcross, E. K. U. Gross, and S. Sharma, "Laser-induced intersite spin transfer," *Nano Letters* **18**, 1842–1848 (2018), pMID: 29424230, <https://doi.org/10.1021/acs.nanolett.7b05118>.
- <sup>8</sup>F. Siegrist, J. A. Gessner, M. Ossiander, C. Denker, Y. P. Chang, M. C. Schröder, A. Guggenmos, Y. Cui, J. Walowski, U. Martens, J. K. Dewhurst, U. Kleineberg, M. Münzenberg, S. Sharma, and M. Schultze, "Light-wave dynamic control of magnetism," *Nature* (2019), 10.1038/s41586-019-1333-x.
- <sup>9</sup>M. Hofherr, S. Häuser, J. K. Dewhurst, P. Tengdin, S. Sakshath, H. T. Nembach, S. T. Weber, J. M. Shaw, T. J. Silva, H. C. Kapteyn, M. Cinchetti, B. Rethfeld, M. M. Murnane, D. Steil, B. Stadtmüller, S. Sharma, M. Aeschlimann, and S. Mathias, "Ultrafast optically induced spin transfer in ferromagnetic alloys," *Science Advances* **6**, 1–8 (2020).
- <sup>10</sup>F. Willems, C. von Korff Schmising, C. Strüber, D. Schick, D. W. Engel, J. K. Dewhurst, P. Elliott, S. Sharma, and S. Eisebitt, "Optical inter-site spin transfer probed by energy and spin-resolved transient absorption spectroscopy," *Nature Communications* **11**, 1–7 (2020).
- <sup>11</sup>J. Chen, U. Bovensiepen, A. Eschenlohr, T. Müller, P. Elliott, E. K. Gross, J. K. Dewhurst, and S. Sharma, "Competing Spin Transfer and Dissipation at Co/Cu (001) Interfaces on Femtosecond Timescales," *Physical Review Letters* **122**, 67202 (2019), arXiv:1803.03090.
- <sup>12</sup>P. Tengdin, C. Gentry, A. Blonsky, D. Zusin, M. Gerrity, L. Hellbrück, M. Hofherr, J. Shaw, Y. Kvashnin, E. K. Delczeg-Czirjak, M. Arora, H. Nembach, T. J. Silva, S. Mathias, M. Aeschlimann, H. C. Kapteyn, D. Thonig, K. Koumpouras, O. Eriksson, and M. M. Murnane, "Direct light-induced spin transfer between different elements in a spintronic Heusler material via femtosecond laser excitation," *Science Advances* **6**, 1–8 (2020).
- <sup>13</sup>D. Steil, J. Walowski, F. Gerhard, T. Kiessling, D. Ebke, A. Thomas, T. Kubota, M. Oogane, Y. Ando, J. Otto, A. Mann, M. Hofherr, P. Elliott, J. K. Dewhurst, G. Reiss, L. Molenkamp, M. Aeschlimann, M. Cinchetti, M. Münzenberg, S. Sharma, and S. Mathias, "Efficiency of ultrafast optically induced spin transfer in heusler compounds," *Phys. Rev. Research* **2**, 023199 (2020).
- <sup>14</sup>I. Radu, K. Vahaplar, C. Stamm, T. Kachel, N. Pontius, H. A. Dürr, T. A. Ostler, J. Barker, R. F. L. Evans, R. W. Chantrell, A. Tsukamoto, A. Itoh, A. Kirilyuk, T. Rasing, and A. V. Kimel, "Transient ferromagnetic-like state mediating ultrafast reversal of antiferromagnetically coupled spins," *Nature* **472**, 205–208 (2011), number: 7342 Publisher: Nature Publishing Group.
- <sup>15</sup>C. La-O-Vorakiat, E. Turgut, C. A. Teale, H. C. Kapteyn, M. M. Murnane, S. Mathias, M. Aeschlimann, C. M. Schneider, J. M. Shaw, H. T. Nembach, and T. J. Silva, "Ultrafast demagnetization measurements using extreme ultraviolet light: Comparison of electronic and magnetic contributions," *Phys. Rev. X* **2**, 011005 (2012).
- <sup>16</sup>C. La-O-Vorakiat, M. Siemens, M. M. Murnane, H. C. Kapteyn, S. Mathias, M. Aeschlimann, P. Grychtol, R. Adam, C. M. Schneider, J. M. Shaw, H. Nembach, and T. J. Silva, "Ultrafast demagnetization dynamics at the *m* edges of magnetic elements observed using a tabletop high-harmonic soft x-ray source," *Phys. Rev. Lett.* **103**, 257402 (2009).
- <sup>17</sup>S. Jana, R. S. Malik, Y. O. Kvashnin, I. L. M. Locht, R. Knut, R. Stefanuik, I. Di Marco, A. N. Yaresko, M. Ahlberg, J. Åkerman, R. Chimata, M. Battiato, J. Söderström, O. Eriksson, and O. Karis, "Analysis of the linear relationship between asymmetry and magnetic moment at the M edge of 3 d transition metals," *Physical Review Research* **2**, 013180 (2020).
- <sup>18</sup>S. Jana, J. A. Terschlüsen, R. Stefanuik, S. Plogmaker, S. Troisi, R. S. Malik, M. Svanqvist, R. Knut, J. Söderström, and O. Karis, "A setup for element specific magnetization dynamics using the transverse magneto-optic kerr effect in the energy range of 30-72 eV," *Review of Scientific Instruments* **88**, 033113 (2017).
- <sup>19</sup>K. Yao, F. Willems, C. von Korff Schmising, C. Strüber, P. Hessing, B. Pfau, D. Schick, D. Engel, K. Gerlinger, M. Schneider, and S. Eisebitt, "A tabletop setup for ultrafast helicity-dependent and element-specific absorption spectroscopy and scattering in the extreme ultraviolet spectral range," *Review of Scientific Instruments* **91**, 093001 (2020), publisher: American Institute of Physics.
- <sup>20</sup>R. Geneaux, H. J. B. Marroux, A. Guggenmos, D. M. Neumark, and S. R. Leone, "Transient absorption spectroscopy using high harmonic generation: a review of ultrafast X-ray dynamics in molecules and solids," *Philosophical Transactions of the Royal Society A: Mathematical, Physical and Engineering Sciences* **377**, 20170463 (2019).
- <sup>21</sup>M. Lewenstein, P. Balcou, M. Y. Ivanov, A. L'Huillier, and P. B. Corkum, "Theory of high-harmonic generation by low-frequency laser fields," *Physical Review A* **49**, 2117–2132 (1994).
- <sup>22</sup>T. Popmintchev, M.-C. Chen, P. Arpin, M. M. Murnane, and H. C. Kapteyn, "The attosecond nonlinear optics of bright coherent X-ray generation," *Nat. Photon.* **4**, 822 (2010).
- <sup>23</sup>W. Ackermann, G. Asova, V. Ayvazyan, A. Azima, N. Baboi, J. Bähr, V. Balandin, B. Beutner, A. Brandt, A. Bolzmann, R. Brinkmann, O. I. Brovko, M. Castellano, P. Castro, L. Catani, E. Chiadroni, S. Choroba, A. Cianchi, J. T. Costello, D. Cubaynes, J. Dardis, W. Decking, H. Delsim-Hashemi, A. Delserieys, G. Di Pirro, M. Dohlus, S. Düsterer, A. Eckhardt, H. T. Edwards, B. Faatz, J. Feldhaus, K. Flöttmann, J. Frisch, L. Fröhlich, T. Garvey, U. Gensch, C. Gerth, M. Görler, N. Golubeva, H.-J. Grabosch, M. Grecki, O. Grimm, K. Hacker, U. Hahn, J. H. Han, K. Honkavaara, T. Hott, M. Hüning, Y. Ivanisenko, E. Jaeschke, W. Jalmuzna, T. Jezynski, R. Kammering, V. Katalev, K. Kavanagh, E. T. Kennedy, S. Khodyachykh, K. Klose, V. Kocharyan, M. Körfer, M. Kollwe, W. Koprek, S. Korepanov, D. Kostin, M. Krassilnikov, G. Kube, M. Kuhlmann, C. L. S. Lewis, L. Lilje, T. Limberg, D. Lipka, F. Löhler, H. Luna, M. Luong, M. Martins, M. Meyer, P. Michelato, V. Miltchev, W. D. Möller, L. Monaco, W. F. O. Müller, O. Napieralski, O. Napoly, P. Nicolosi, D. Nölle, T. Nuñez, A. Oppelt, C. Pagani, R. Paparella, N. Pchalek, J. Pedregosa-Gutierrez, B. Petersen,

- B. Petrosyan, G. Petrosyan, L. Petrosyan, J. Pflüger, E. Plönjes, L. Poletto, K. Pozniak, E. Prat, D. Proch, P. Pucyk, P. Radcliffe, H. Redlin, K. Rehlich, M. Richter, M. Roehrs, J. Roensch, R. Romaniuk, M. Ross, J. Rossbach, V. Rybnikov, M. Sachwitz, E. L. Saldin, W. Sandner, H. Schlarb, B. Schmidt, M. Schmitz, P. Schmüser, J. R. Schneider, E. A. Schneidmiller, S. Schnepp, S. Schreiber, M. Seidel, D. Sertore, A. V. Shabunov, C. Simon, S. Simrock, E. Sombrowski, A. A. Sorokin, P. Spanknebel, R. Spesyvtsev, L. Staykov, B. Steffen, F. Stephan, F. Stulle, H. Thom, K. Tiedtke, M. Tischer, S. Toleikis, R. Treusch, D. Trines, I. Tsakov, E. Vogel, T. Weiland, H. Weise, M. Wellhöfer, M. Wendt, I. Will, A. Winter, K. Wittenburg, W. Wurth, P. Yeates, M. V. Yurkov, I. Zagorodnov, and K. Zapfe, "Operation of a free-electron laser from the extreme ultraviolet to the water window," *Nature Photonics* **1**, 336–342 (2007), number: 6 Publisher: Nature Publishing Group.
- <sup>24</sup>R. W. Schoenlein, "Generation of Femtosecond Pulses of Synchrotron Radiation," *Science* **287**, 2237–2240 (2000).
- <sup>25</sup>A. A. Zholents and M. S. Zolotarev, "Femtosecond X-Ray Pulses of Synchrotron Radiation," *Physical Review Letters* **76**, 912–915 (1996).
- <sup>26</sup>W. Boutu, M. Ducouso, J.-F. Hergott, and H. Merdji, "Overview on HHG High-Flux Sources," in *Optical Technologies for Extreme-Ultraviolet and Soft X-ray Coherent Sources*, Springer Series in Optical Sciences, edited by F. Canova and L. Poletto (Springer, Berlin, Heidelberg, 2015) pp. 63–78.
- <sup>27</sup>S. Hädrich, J. Rothhardt, M. Krebs, S. Demmler, A. Klenke, A. Tünnermann, and Jens Limpert, "Single-pass high harmonic generation at high repetition rate and photon flux," *Journal of Physics B: Atomic, Molecular and Optical Physics* **49**, 172002 (2016).
- <sup>28</sup>S. Yamamoto and I. Matsuda, "Measurement of the resonant magneto-optical kerr effect using a free electron laser," *Applied Sciences* **7** (2017), 10.3390/app7070662.
- <sup>29</sup>A. Yaresko, A. Perlov, V. Antonov, and B. Harmon, "Band-Structure Theory of Dichroism," in *Magnetism: A Synchrotron Radiation Approach*, Lecture Notes in Physics, edited by E. Beaurepaire, H. Bulou, F. Scheurer, and J.-P. Kappler (Springer, Berlin, Heidelberg, 2006) pp. 121–141.
- <sup>30</sup>M. Hecker, P. M. Oppeneer, S. Valencia, H. C. Mertins, and C. M. Schneider, "Soft X-ray magnetic reflection spectroscopy at the 3p absorption edges of thin Fe films," *Journal of Electron Spectroscopy and Related Phenomena Proceeding of the Fourteenth International Conference on Vacuum Ultraviolet Radiation Physics*, **144-147**, 881–884 (2005).
- <sup>31</sup>M. Pretorius, J. Friedrich, A. Ranck, M. Schroeder, J. Voss, V. Wedemeier, D. Spanke, D. Knabben, I. Rozhko, H. Ohldag, F. U. Hillebrecht, and E. Kisker, "Transverse magneto-optical Kerr effect of Fe at the Fe 3p threshold," *Phys. Rev. B* **55**, 14133–14135 (1997), publisher: American Physical Society.
- <sup>32</sup>O. Pronin, V. Pervak, E. Fill, J. Rauschenberger, F. Krausz, and A. Apolonski, "Ultrabroadband efficient intracavity XUV output coupler," *Opt. Express* **19**, 10232–10240 (2011), publisher: OSA.
- <sup>33</sup>F. Frassetto, C. Cacho, C. A. Froud, I. E. Turcu, P. Villoresi, W. A. Bryan, E. Springate, and L. Poletto, "Single-grating monochromator for extreme-ultraviolet ultrashort pulses," *Optics Express* **19**, 19169 (2011).
- <sup>34</sup>W. Cash, "Echelle spectrographs at grazing incidence," *Applied Optics* **21**, 710–717 (1982), publisher: Optical Society of America.
- <sup>35</sup>M. Imada, A. Fujimori, and Y. Tokura, "Metal-insulator transitions," *Reviews of modern physics* **70**, 1039 (1998).
- <sup>36</sup>Y. Tokura and Y. Tomioka, "Colossal magnetoresistive manganites," *Journal of magnetism and magnetic materials* **200**, 1–23 (1999).
- <sup>37</sup>V. Moshnyaga and K. Samwer, "Ferromagnetic manganite films," *Handbook of Magnetism and Advanced Magnetic Materials* (2007).
- <sup>38</sup>S. Eich, M. Plötzing, M. Rollinger, S. Emmerich, R. Adam, C. Chen, H. C. Kapteyn, M. M. Murnane, L. Plucinski, D. Steil, B. Stadtmüller, M. Cinchetti, M. Aeschlimann, C. M. Schneider, and S. Mathias, "Band structure evolution during the ultrafast ferromagnetic-paramagnetic phase transition in cobalt," *Science Advances* **3** (2017), 10.1126/sciadv.1602094.
- <sup>39</sup>R. Gort, K. Bühlmann, G. Saerens, S. Däster, A. Vaterlaus, and Y. Acremann, "Ultrafast magnetism: The magneto-optical kerr effect and conduction electrons," *Applied Physics Letters* **116**, 112404 (2020), <https://doi.org/10.1063/1.5143115>.
- <sup>40</sup>M. Hennes, B. Rösner, V. Chardonnet, G. S. Chiuzaian, R. Delaunay, F. Döring, V. A. Guzenko, M. Hehn, R. Jarrier, A. Kleibert, M. Lebugle, J. Lüning, G. Malinowski, A. Merhe, D. Naumenko, I. P. Nikolov, I. Lopez-Quintas, E. Pedersoli, T. Savchenko, B. Watts, M. Zangrando, C. David, F. Capotondi, B. Vodungbo, and E. Jal, "Time-resolved xuv absorption spectroscopy and magnetic circular dichroism at the ni m<sub>2,3</sub>-edges," *Applied Sciences* **11** (2021), 10.3390/app11010325.
- <sup>41</sup>K. Yao, F. Willems, C. von Korff Schmising, I. Radu, C. Strüber, D. Schick, D. Engel, A. Tsukamoto, J. K. Dewhurst, S. Sharma, and S. Eisebitt, "Distinct spectral response in *m*-edge magnetic circular dichroism," *Phys. Rev. B* **102**, 100405 (2020).
- <sup>42</sup>S. Mathias, C. La-O-Vorakiat, P. Grychtol, P. Granitzka, E. Turgut, J. M. Shaw, R. Adam, H. T. Nembach, M. E. Siemens, S. Eich, C. M. Schneider, T. J. Silva, M. Aeschlimann, M. M. Murnane, and H. C. Kapteyn, "Probing the timescale of the exchange interaction in a ferromagnetic alloy," *Proceedings of the National Academy of Sciences* **109**, 4792–4797 (2012).
- <sup>43</sup>S. Günther, C. Spezzani, R. Ciprian, C. Grazioli, B. Ressel, M. Coreno, L. Poletto, P. Miotti, M. Sacchi, G. Panaccione, V. c. v. Uhlř, E. E. Fullerton, G. De Ninno, and C. H. Back, "Testing spin-flip scattering as a possible mechanism of ultrafast demagnetization in ordered magnetic alloys," *Phys. Rev. B* **90**, 180407 (2014).
- <sup>44</sup>M. Jungbauer, S. Hühn, R. Egoavil, H. Tan, J. Verbeeck, G. Van Tendeloo, and V. Moshnyaga, "Atomic layer epitaxy of ruddlesden-popper sro (sr<sub>10</sub>)<sub>3</sub> n films by means of metalorganic aerosol deposition," *Applied Physics Letters* **105**, 251603 (2014).